Materials Science & Engineering A 640 (2015) 82–90

Contents lists available at ScienceDirect

Materials Science & Engineering A

journal homepage: www.elsevier.com/locate/msea

Effect of alloying addition and microstructural parameters on mechanical properties of 93% tungsten heavy alloys

U. Ravi Kiran [a,*], A. Panchal [a], M. Sankaranarayana [a], G.V.S. Nageswara Rao [b], T.K. Nandy [a]

[a] Defence Metallurgical Research Laboratory, Kanchanbagh, Hyderabad 500 058, India
[b] National Institute of Technology, Warangal 506004, India

ARTICLE INFO

Article history:
Received 3 February 2015
Received in revised form
15 May 2015
Accepted 16 May 2015
Available online 22 May 2015

Keywords:
Tungsten heavy alloy
Swaging
Tensile properties
Impact strength
Fractography

ABSTRACT

Liquid phase sintering, heat treatment and swaging studies on three tungsten heavy alloys, 93W–4.9Ni–2.1Fe (wt%), 93W–4.2Ni–1.2Fe–1.6Co (wt%) and 93W–4.9Ni–1.9Fe–0.2Re (wt%) were carried out in detail with respect to microstructure, tensile and impact properties. All the alloys were sintered and swaged to 40% deformation. The results indicate that Re addition reduces the grain size of the alloy compared to W–Ni–Fe and W-Ni-Fe-Co alloys. W–Ni–Fe–Re alloy shows superior tensile properties in heat treated condition as compared to W–Ni–Fe and W–Ni–Fe–Co alloys. SEM study of fractured specimens clearly indicates that the failure in case of W–Ni–Fe–Re was due to transgranular cleavage of tungsten grains and W–W de-cohesion. W–Ni–Fe and W–Ni–Fe–Co alloys also failed by mixed mode failure. However, in these cases, ductile dimples corresponding the failure of the matrix phase was rarely seen. Thermo-mechanical processing resulted in significant changes in mechanical properties. While W–Ni–Fe–Re alloy showed the highest tensile strength (1380 MPa), W–Ni–Fe–Co exhibited the highest elongation (12%) to failure. A detailed analysis involving microstructure, mechanical properties and failure behavior was undertaken in order to understand the property trends.

1. Introduction

Tungsten alloys have found increasing applications in kinetic energy penetrators, radiation shielding, balance weights and electrical contacts due to high density, good physical and mechanical properties [1–3]. Tungsten heavy alloys (WHA), prepared by liquid-phase sintering, are composite materials in which quasi-spherical shaped hard bcc particles are embedded in the ductile Ni–Fe–W solid solution fcc matrix. Liquid phase sintering (LPS) offers advantages of relatively low sintering temperature, enhanced densification, microstructural homogenization and near theoretical sintered densities. In addition, LPS also enables high material utilization (> 95%), near-net shaping, high productivity, and superior properties [4]. Tungsten heavy alloys offer a unique combination of properties such as high density (16–18 g/cm^3), high strength (1000–1700 MPa), high ductility (10–30%), good corrosion resistance, and easy machinability. One of the strategic applications for these alloys is in ordnance, such as kinetic-energy (KE) penetrators. While the high density of tungsten heavy alloy helps in realization of higher depth of penetration, their excellent mechanical properties such as high strength, ductility and impact property ensure the survival of penetrator from the rigors of extremely demanding conditions experienced during their launch and terminal ballistics [5]. The as-sintered WHAs are generally vacuum-annealed followed by oil quenching to remove trapped hydrogen, ensure homogenization of the matrix and also reduce the interfacial segregation of impurities [6–8]. Mechanical properties of the sintered heavy alloys can be further improved by thermomechanical processing that involves repeated heat treatment and swaging. Islam et al. [9] conducted experiments on heat treated W–Ni–Fe alloys and showed that the binding strength between W and the matrix phase has a major influence on the ductility of WHAs. This can be addressed by either heat treatment or suitable alloying additions. Increasing tungsten (> 93%) results in increase in the density of the alloy leading to higher depth of penetration. However, the alloys containing higher tungsten exhibit inferior mechanical properties [10,11]. Since, 90% W with nickel and iron are widely used composition and alloys with higher tungsten have received less attention, it was decided to study alloys with 93% tungsten base alloys with minor additions of Co and Re and correlate mechanical properties with underlying microstructure. Although W alloys with improved mechanical properties were successfully developed [10–13], limited results are available on the effect of higher tungsten content (93%) alloys on tensile and Charpy impact properties in the thermo-mechanically processed condition [14]. In the present investigation, WHAs that

* Corresponding author. Fax: +91 4024346447.
E-mail address: uravikiran@gmail.com (U. Ravi Kiran).

http://dx.doi.org/10.1016/j.msea.2015.05.046
0921-5093/

comprise about 93% W and balance matrix alloy containing Ni, Fe, Co and Re have been investigated in detail with respect to microstructure, tensile properties and impact toughness. The effect of relative volume fraction of tungsten and the matrix phase on mechanical properties of heavy alloys have also been discussed.

2. Experimental

Three tungsten heavy alloys, namely WNF (93W–4.9Ni–2.1Fe), WNC (93W–4.2Ni–1.2Fe–1.6Co) and WNR (93W–4.9Ni–1.9Fe–0.2Re) were prepared by powder metallurgy route. The characteristics of the initial powders used in the present study are shown in Table 1. Tungsten powder was admixed with elemental powders such as Ni, Fe, Co and Re in the required proportions using a ball mill with BPR (Ball to Powder Ratio) 2:1 at a speed of 50 rpm for 48 h. The mixed powders were then filled in a 55 mm diameter and 400 mm length PVC mold and cold iso-statically pressed (Make: National Forge, Belgium) at 250 MPa pressure for 20 min. The cold pressed tungsten heavy alloy rods were sintered in a hydrogen sintering furnace (Therelek Furnace, Hyderabad, India) at a temperature of 1480 °C for 2 h. The sintering cycle employed for the present study is shown in Fig.1. The densities of the sintered blanks were measured with the Archimedes water immersion method. The sintered tungsten heavy alloy blanks were subjected to vacuum heat treatment (1100 °C/2 h/oil quench) followed by swaging (20%), vacuum heat treatment (1100 °C/2 h/oil quench) and final swaging to 40% reduction.

Samples were prepared for microstructural evaluation by standard metallographic procedures involving cutting, mounting, grinding and polishing. The size of the tungsten grains, volume fraction of the matrix phase, contiguity of the sintered WHAs were measured from scanning electron micrographs taken from several locations of a specimen. The volume fraction was measured using an image analyzing software. The grain size data was acquired by determining the area of the grain, then by assuming a spherical grain, the equivalent diameter was calculated. The co-ordination number was measured using the following method. One grain from scanning micrograph was selected, and the number of grains that are in contact with it are counted. The process is repeated over several grains. A minimum of 500 grains were used for all microstructural measurements. The co-ordination number reported is an average of those values. Contiguity defined as the relative fraction of W–W interfacial area was determined by placing grid lines over the binary image and counting the number of tungsten–tungsten and tungsten–matrix intercepts. It was calculated using the equation

$$\left(CSS = 2N_{SS}/(2N_{SS} + N_{SL})\right) \quad (1)$$

where N_{SS} and N_{SL} are the number of W–W grain boundary and W–matrix interface boundary intercepted, respectively.

EDAX analysis of the matrix composition of all the alloys was also carried out using Scanning Electron Microscope. All the swaged samples were subjected to tensile testing. The tensile specimens were prepared as per ASTM standard T-145 and tested at room temperature using universal tensile testing machine (INSTRON 5500R, UK). Three specimens for each condition were tested at a cross speed of 1 mm/min which results in the strain rate of 6.6×10^{-4}. Charpy impact specimens were prepared as per ASTM standards (E23) [15] and evaluation was carried out in a pendulum type impact tester at room temperature. Fractography of the failed tensile and impact test pieces were carried out using Scanning electron microscope (Make: FEI, Quanta-400, Netherlands). Bulk hardness of the alloys was measured using Vickers hardness tester (Vickers Instruments, Model: 1965, UK). All tests were conducted at a load of 30 kg and indentation time of 30 s was maintained. The Vickers hardness value for each sample was an average of five readings taken at random locations throughout the sample of 10×10 mm^2 area. Micro-hardness of the tungsten grains and the matrix phase in as swaged condition were measured separately by micro-hardness tester (Make: MAT-SUZAWA, Japan).

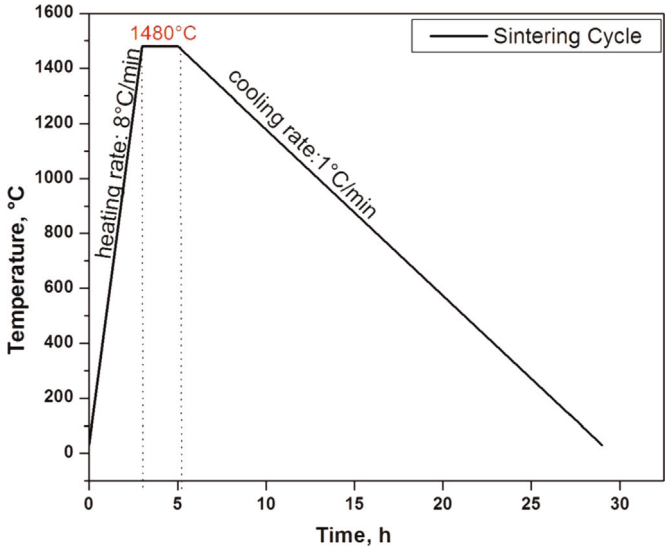

Fig. 1. Sintering cycle for the heavy alloys.

3. Results and discussion

3.1. Microstructure

Scanning electron micrographs of the sintered tungsten heavy alloys are shown in Fig. 2. As can be seen, the tungsten particles in WNF (Fig. 2a) and WNC (Fig. 2b) are coarser than those in WNR (Fig. 2c). The difference is attributable to the difference in solubility of tungsten in the matrix phase of the alloys. The final grain size is a result of Ostwald ripening that results in the coarsening of grains with the volume fraction of liquid phase remaining

Table 1
Characteristics of the powders used in the present study

Powder	W	Ni	Fe	Co	Re
Vendor	Blue star metals	Blue star metals	Blue star metals	Electronica	Corporate associates
Purity, wt%	99.9	99.6	99.6	99.6	99.5
Fabrication method	Reduction	Carbonyl	Atomization	Reduction	Reduction
Particle size (d_{50}), μm	8	6	5	4	12
Shape	Cuboid	Spherical	Spherical	Irregular	Irregular
Theoretical density (g/cm^3)	19.3	8.9	8.9	8.8	20.8
Apparent density (g/cm^3)	4.8	1.0	3.2	2.2	-
Tap density (g/cm^3)	5.8	1.4	3.5	2.8	-

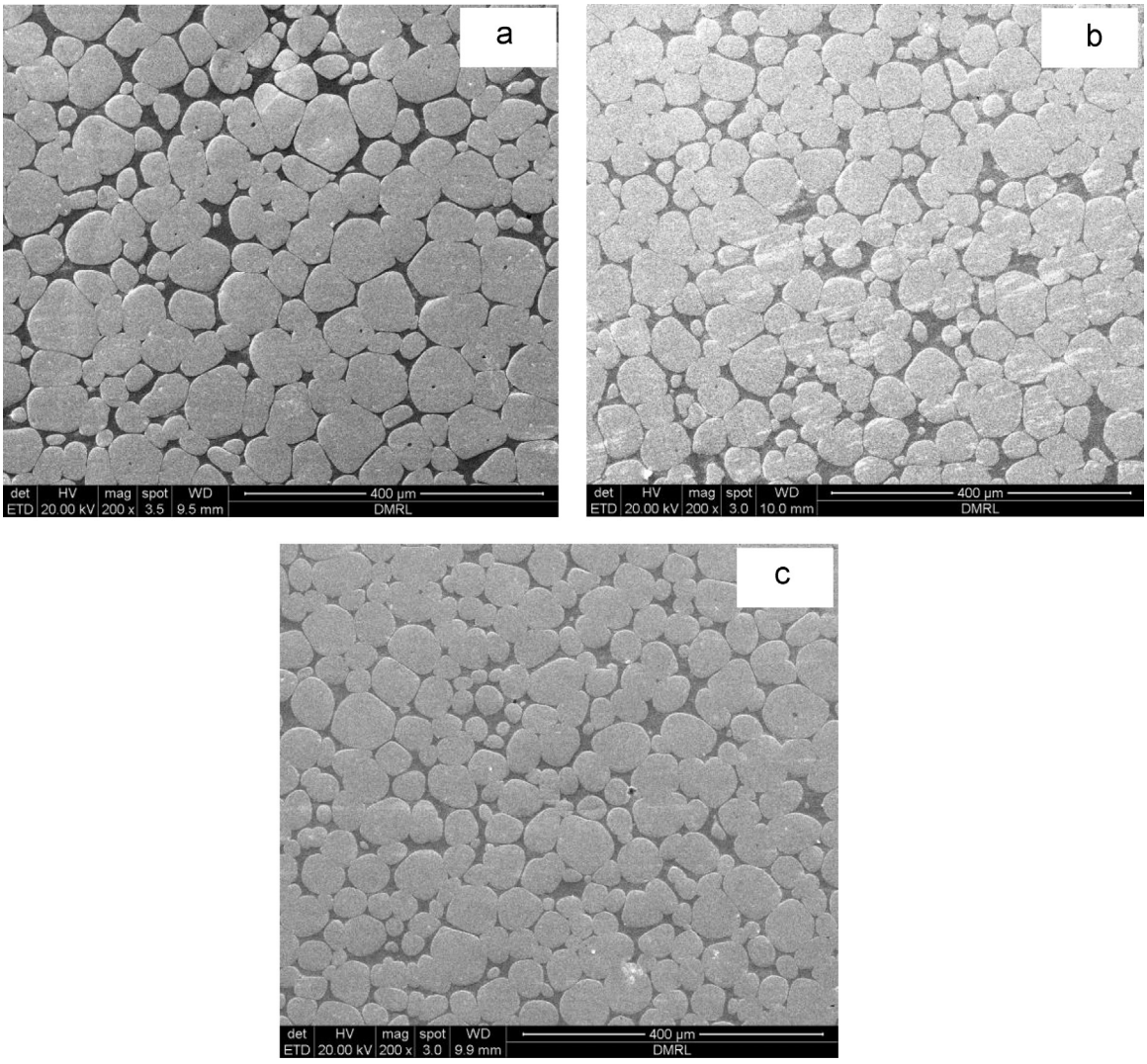

Fig. 2. Scanning electron micrographs of (a) WNF, (b) WNC, and (c) WNR heavy alloys.

constant. Grain size variation with respect to three tungsten heavy alloys are presented in Fig. 3. Addition of rhenium to the alloy (WNR) reduces the grain size considerably. Rhenium addition is expected to suppress the Ostwald ripening process by reducing W-solubility in the matrix liquid and inhibiting W-grains from solution-precipitation-growth [16]. This is further supported with EDS analysis carried out on the matrix phase of the alloys. Table 2 shows the EDS analysis of mean composition of matrix and tungsten phases for all three alloys. The tungsten solubility for rhenium contain alloy in the matrix phase was 24%. This solubility is lower than that obtained in WNF (27.5 wt%) and WNC (34 wt%) alloys. Thus, the analysis shows that rhenium controls the grain growth especially by reducing the solid solubility of tungsten in the liquid, resulting in slower grain growth.

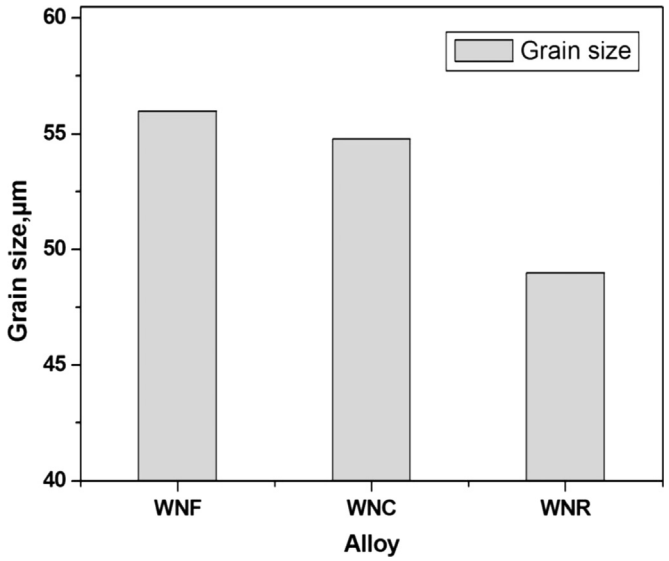

Fig. 3. Grain size variation in tungsten heavy alloys.

Table 3 summarizes the microstructural parameters of the alloys. It is noted that tungsten solubility and matrix volume fraction increase (Fig. 4), while dihedral angle and the co-ordination number (Fig. 5) decrease in the WNC alloy in comparison to the WNF and WNR alloys. It is believed that increase in tungsten solubility in the matrix lowers the solid–liquid surface energy, which leads to grain boundary penetration. Thus, the decrease in solid–liquid surface energy causes decrease in dihedral angle and co-ordination of tungsten particles [17]. The decrease in dihedral angle will lead to decrease in neck size according to the relation [4]:

$$X = G \sin \phi/2 \quad (2)$$

Table 2
EDS analysis of chemical compositions of W and matrix phases of sintered plus heat treated samples (wt%).

Alloy	Chemical composition(%)	W phase					Matrix phase				
		W	Ni	Fe	Co	Re	W	Ni	Fe	Co	Re
WNF	Min	98.88	0.18	0.18	–	–	26.61	51.21	21.19	–	–
	Max	99.45	0.25	0.38	–	–	27.13	51.68	21.64	–	–
	Mean	99.23	0.23	0.27	–	–	27.53	51.32	21.42	–	–
WNC	Min	99.25	0.04	0.52	0.02	–	32.16	38.78	10.21	14.86	–
	Max	99.99	0.07	0.98	0.06	–	35.99	40.12	11.04	16.68	–
	Mean	99.50	0.05	0.85	0.04	–	33.85	39.42	10.37	16.27	–
WNR	Min	99.02	0.18	0.18	–	0.01	24.23	20.46	50.67	–	1.61
	Max	99.86	0.25	0.38	–	0.03	25.21	22.86	52.39	–	1.50
	Mean	99.65	0.23	0.27	–	0.02	24.72	21.10	52.00	–	1.55

Table 3
Microstructural parameters of tungsten alloys.

Alloy	Tungsten grain size (μm)	Volume fraction of matrix (Pct)	Contiguity	Dihedral angle	Co-ordination number	Matrix mean path (μm)
WNF	56	0.14	0.53 ± 0.05	51 ± 1	2.49	3.03
WNC	54	0.17	0.43 ± 0.01	46 ± 2	2.10	3.42
WNR	49	0.16	0.48 ± 0.06	62 ± 2	2.74	3.04

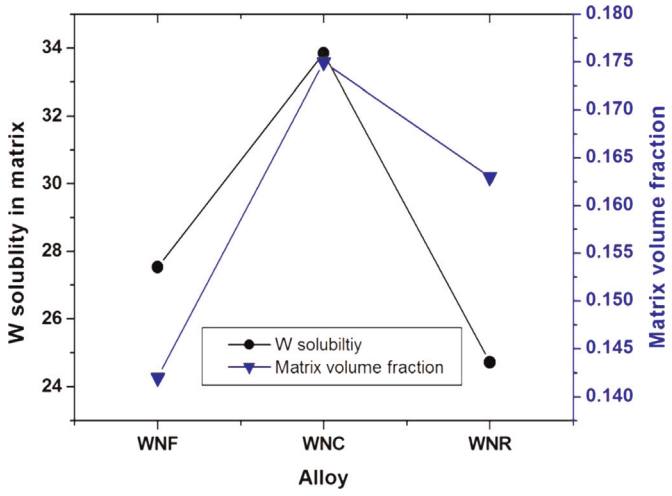

Fig. 4. Tungsten solubility and matrix volume fraction in tungsten alloys.

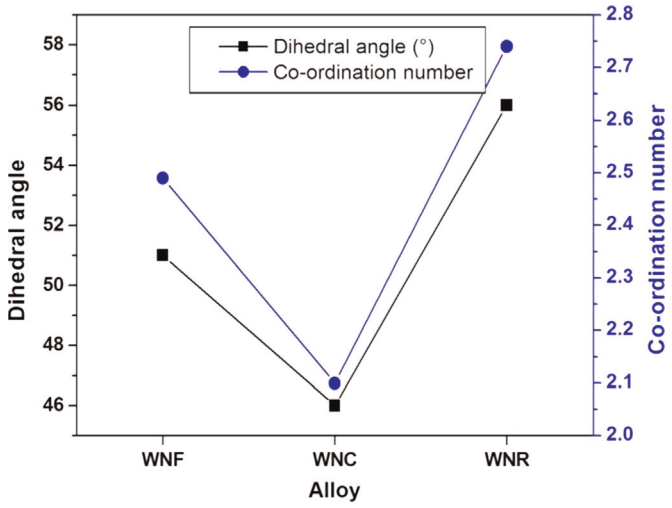

Fig. 5. Dihedral angle and Co-ordination number variation in tungsten alloys.

where X is the neck size between grains, G the grain size, and φ the dihedral angle.

Fig. 6 shows the influence of swaging on microstructure for the alloys. It is evident after swaging, the aspect ratio of tungsten grains has increased along the swaging direction for all the alloys, but the microstructural parameters like contiguity and volume fraction remains constant. The influence of these microstructural parameters on the mechanical properties of the alloys are explained in the following sections.

3.2. Hardness, Tensile and impact strength

The hardness results (Table 5) shows that the bulk hardness of the samples increased marginally with the addition of cobalt and rhenium. It is also observed that the micro-hardness values of the tungsten grains are same in all three alloys. But comparison of micro-hardness of the matrix phase clearly indicates higher hardness of WNC (425 $HV_{0.1}$) alloy as compared to other alloys (412 $HV_{0.1}$ for WNF and 421 $HV_{0.1}$ WNR). This is ascribed to hardening of the matrix phase due to increase in tungsten content in the matrix (Table 2). The difference in hardness, however, is less pronounced as compared to difference in tensile properties of the alloys.

The stress–strain curves of sintered plus heat treated and sintered plus heat treated plus double swaged alloys are substantially different (Figs. 7 and 8). The yield strength values of the heat treated alloys are lower. With plastic deformation, the stress increases rapidly till it reaches the tensile strength followed by immediate failure. On the other hand, the swaged alloys show relatively flatter stress–strain curves with higher yield strength. The higher yield strength in the swaged condition is attributed to the plastic deformation imparted by swaging (40% with an intermediate heat treatment). A log–log plot of true stress vs. true plastic strain (Fig. 11) clearly shows that the work hardening exponents in swaged alloys are substantially lower (Tables 4 and 5). This is due to accumulated dislocations in swaging deformation which reduces the strain hardening rate.

The tensile properties of the alloys in heat treated and thermo-mechanically processed conditions are shown in Tables 4 and 5. In the heat treated condition yield strength value in cobalt containing alloy (WNC) is the lowest while that in rhenium containing alloy (WNR) is the highest. This may be attributed to the mean free path of the softer matrix phase where the initiation of plastic deformation takes place. The yield strength of the two phase tungsten heavy alloy is expressed as

$$\sigma y = \sigma_o + kGb\left(\frac{1 - V_M}{DV_M}\right)^{1/2} \quad (3)$$

where σ_y is the yield strength, σ_o is the intrinsic strength, k is a constant, G is the shear modulus, b is the Burgers vector, D is the

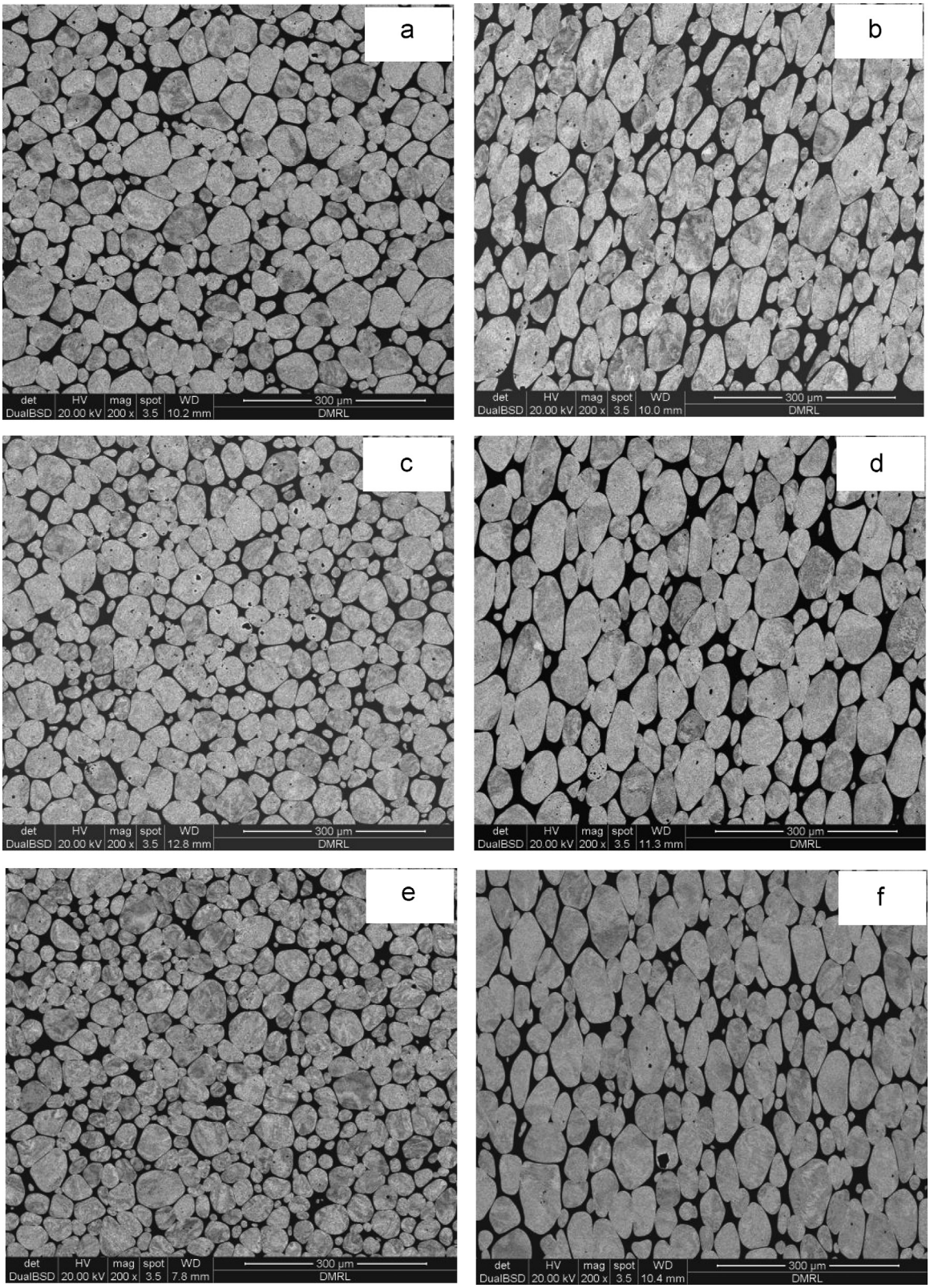

Fig. 6. Back scattered electron micrographs of swaged (a) WNF (transverse), (b) WNF (longitudinal), (c) WNC (transverse), (d) WNC (longitudinal), (e) WNR (transverse), and (f) WNR (longitudinal).

tungsten grain size and V_M is the matrix volume fraction [18].

It must be noted that the last term is the mean free path of the softer phase, i.e., matrix in this case. Thus, lower yield strength in cobalt containing alloy is attributed to its marginally higher mean free path. The same trend is also seen in the swaged alloy. Significant increase in both yield strength and tensile strength in swaged condition as compared to heat treated condition (Tables 4 and 5) is directly attributed to accumulation of dislocations during swaging. Additionally, the difference across the alloys is substantial which may possibly be due to the difference in work

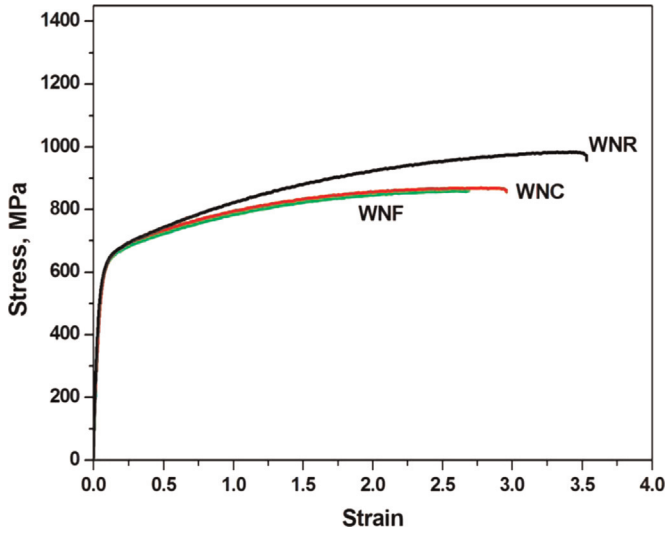

Fig. 7. Stress–strain curves for 93% tungsten heavy alloys (Sintered plus heat treated).

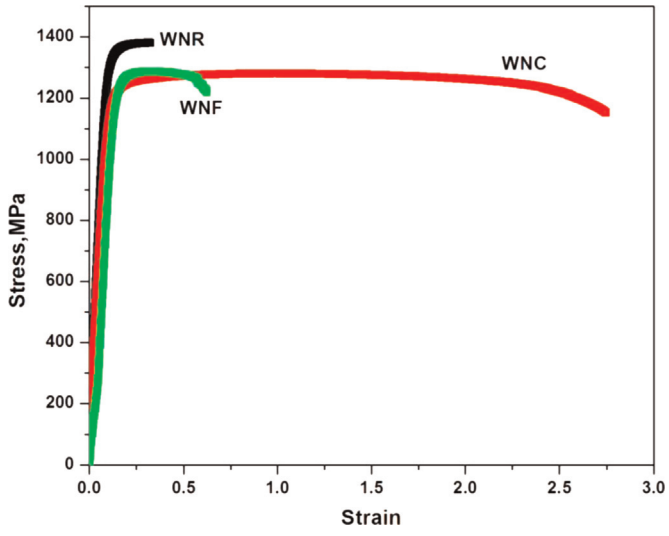

Fig.8. Stress–strain curves for 93% tungsten heavy alloys (after swaging).

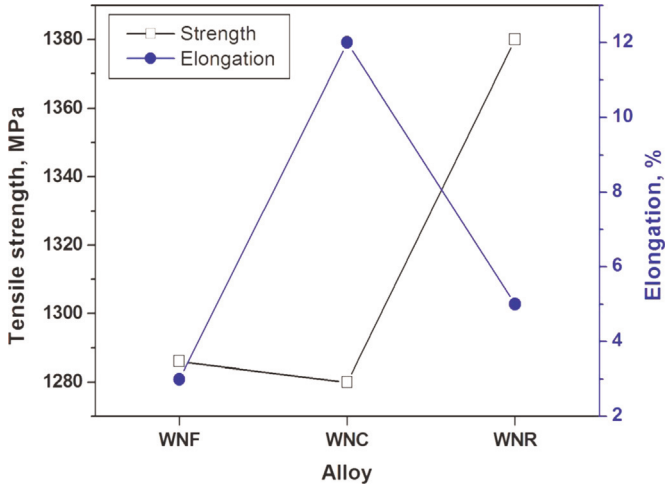

Fig. 9. Tensile properties of heavy alloys after swaging.

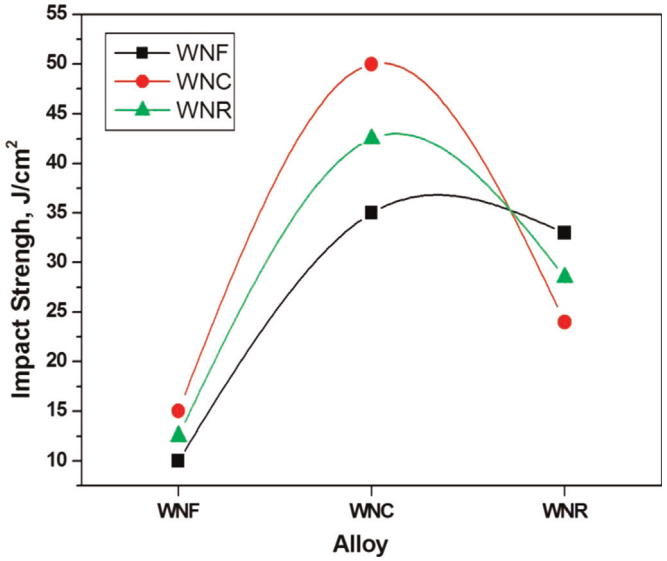

Fig. 10. Impact strength variation in swaged tungsten alloys.

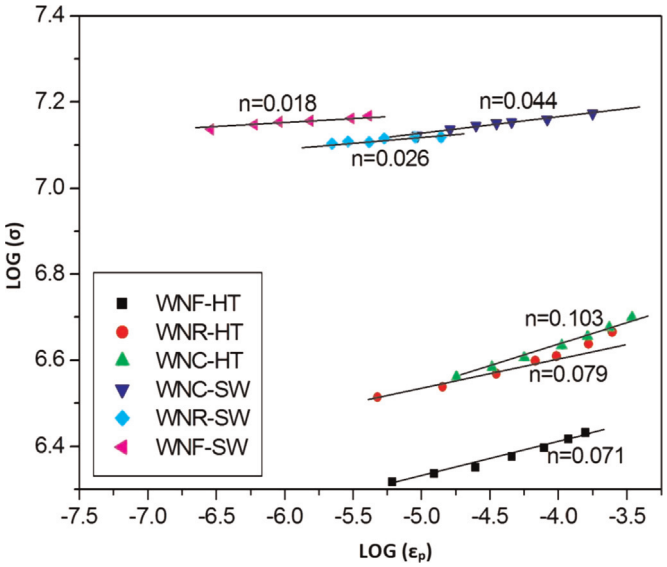

Fig. 11. Log(σ) vs. log(ϵ_p) plots for sintered plus heat treated and swaged specimens. The n values are also mentioned in the plot.

hardening behavior since the alloys have been imparted substantial deformation during swaging.

The tensile strength in heat treated condition vary only marginally across the alloys (858–876 MPa) with WNR showing the highest strength. The elongation values are similar at 17–18%. Following swaging, the tensile strength increases substantially while the elongation drops (Table 5 and Fig. 9). This is attributed to accumulation of dislocations. Again in this case, the rhenium containing alloy shows maximum strength, however at much lower elongation values. Cobalt containing alloy shows the highest elongation at 12%. This is possibly attributed to several reasons: (1) higher solubility of tungsten in the matrix phase, (2) higher matrix volume fraction thereby rendering the matrix stronger (Tables 3), (3) lower contiguity in the alloy (Tables 3) and (4) lower connectivity (Table 3). It is well known that W–W interfaces are the low energy preferred path for crack nucleation. Decreased contiguity or connectivity implies that such crack nucleation sites are less in WNC thereby resulting in greater ductility.

Impact properties (Table 5 and Fig. 10) after swaging clearly show the superiority of cobalt containing alloy. This is consistent with higher elongation values of the alloy. Again relatively higher impact toughness of cobalt containing alloy is due to favorable microstructural features such as higher matrix volume fraction and lower connectivity of tungsten grains. Thus, as a first approximate, it appears % elongation and impact toughness behave similarly.

As metioned earlier, the true stress–strain data were fitted to a power law hardening equation [19]

$$\sigma = K\varepsilon^n \quad (4)$$

where σ is the true stress, ε is true plastic strain, K is strength coefficient, n is a work hardening exponent. The work hardening response of the alloys calculated from true stress–true plastic strain plots are shown in Table 5 and Fig. 11. It clearly indicates that WNC alloy in thermo-mechanically processed condition exhibits higher work hardening rates (0.044) compared to WNF (0.018) and WNR (0.026) alloys. Higher work hardening response in this alloy is a consequence of higher volume fraction of matrix. Following swaging there is a decrease in work hardening behavior.

Table 4
Mechanical properties of alloys after sintering and heat treatment.

Alloy	Tensile strength (MPa)	Yield strength (MPa)	Yield ratio	El (%)	Work hardening exponent (n)
WNF	858	628	0.731	17	0.071
WNC	869	623	0.716	18	0.103
WNR	876	637	0.727	18	0.079

3.3. Fractography

The fracture features of sintered plus heat treated alloys, broken after tensile testing, is shown in Fig. 12. All alloys are characterized by W-matrix and W–W decohesion, tungsten cleavage

Table 5
Mechanical properties after swaging.

Alloy	Tensile strength (MPa)	Yield strength (MPa)	Yield ratio	El (%)	Impact strength (J/cm^2)	Bulk- hardness, VHN	Micro-hardness		Work hardening exponent (n)
							W	Matrix	
WNF	1286	1255	0.975	3	13	510 ± 3	510 ± 1	412 ± 3	0.018
WNC	1280	1219	0.952	12	42	515 ± 3	511 ± 2	425 ± 2	0.044
WNR	1380	1347	0.976	5	26	514 ± 2	509 ± 1	421 ± 3	0.026

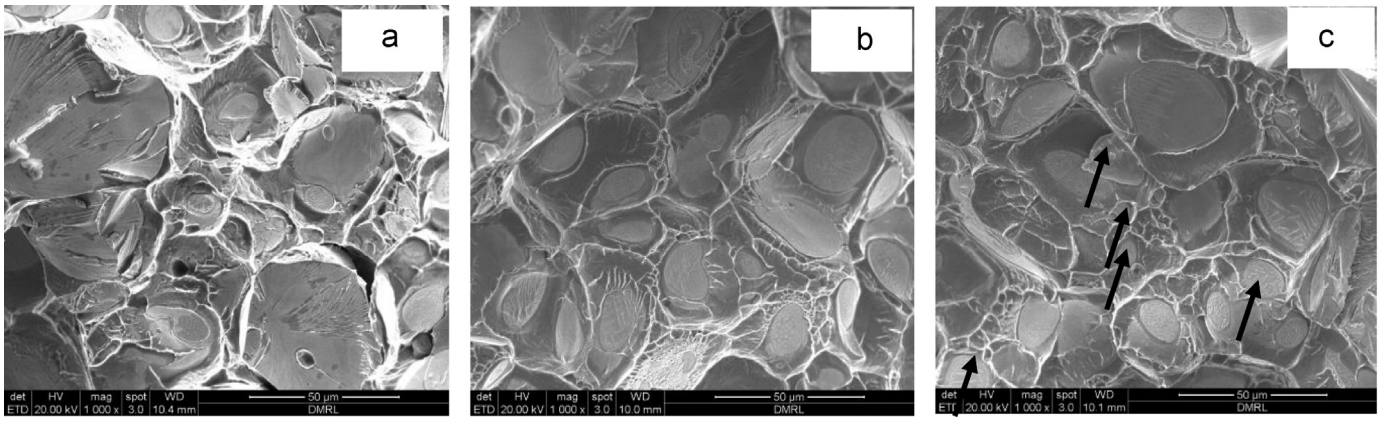

Fig. 12. Tensile fractographs of (a) WNF, (b) WNC, and (c) WNR heavy alloys in sintered plus heat treated condition.

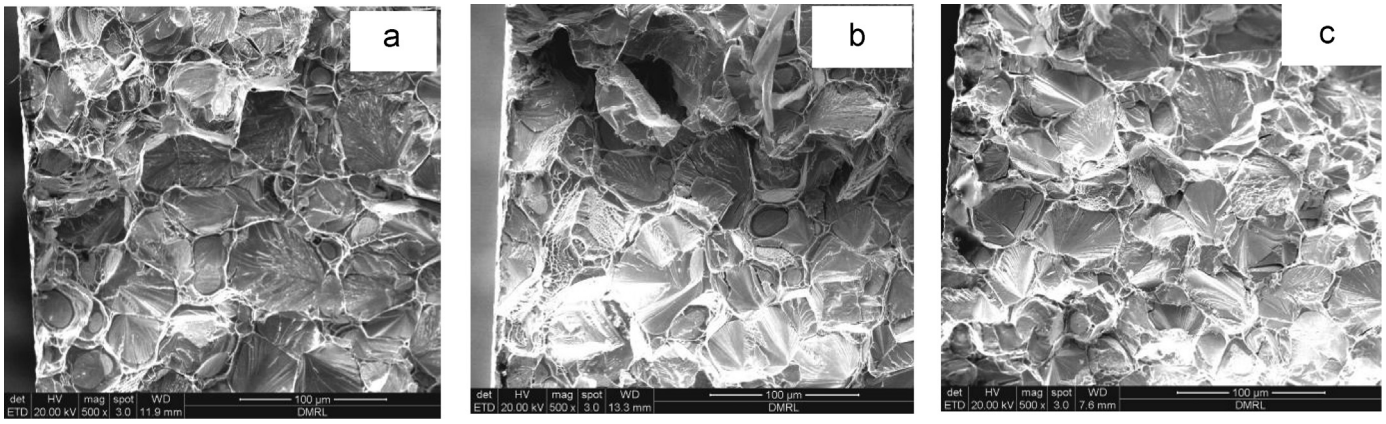

Fig. 13. Tensile fractographs of (a) WNF, (b) WNC, and (c) WNR heavy alloys in swaged condition.

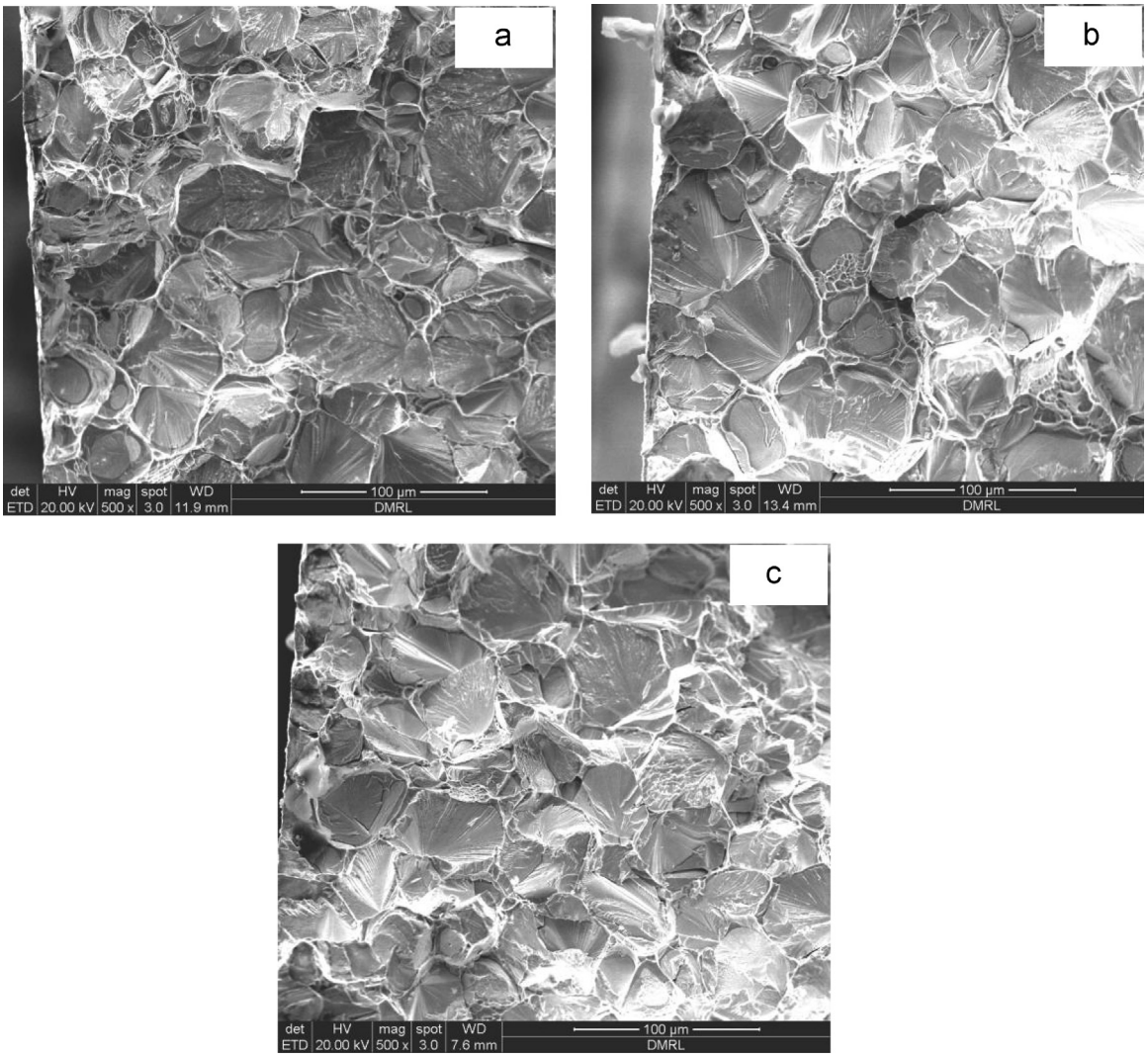

Fig. 14. Impact fractographs of (a) WNF, (b) WNC, and (c) WNR tungsten alloys in swaged condition.

and matrix failure. The rhenium containing alloy (Fig.12c), exhibit relatively finer features. In Fig. 13 the fracture morphology of swaged alloys are shown. In this case fracture is more transgranular failure in nature comprising tungsten cleavage along with matrix failure, although the plastic deformation before fracture was noticeably lower than for the as sintered alloys. Additionally, the features are finer in the swaged alloys. This may be attributed to reduction in the dimensions of microstructural features especially perpendicular to the swaging axis that is parallel to that of tensile axis. WNR exhibits predominant transgranular cleavage of tungsten grains as compared to the other alloys (Fig. 13c) and this is consistent with higher strength realised in these alloys [20]. The cobalt containing alloy exhibits relatively more features corresponding matrix failure than the other alloys, which is shown in Fig. 13b. The fractographs of the impact specimens exhibit predominant transgranular features with those corresponding to Re containing alloy discernibly finer (Fig. 14). Instances of dimples pointing towards matrix failure are seen in Co containing alloy which appears to be consistent with its higher impact energy.

4. Conclusions

In the present study the effect of alloying addition and microstructural parameters on the mechanical properties of 93% tungsten heavy alloys were investigated. The tensile and impact strength of the studied alloys were found to be influenced by their alloy chemistry and microstructural properties. Important conclusions of this study are:

1. Cobalt increases the solid solubility of tungsten in the matrix phase. This leads to increase in the volume fraction of the matrix phase. Rhenium reduces the solid solubility of tungsten in the matrix resulting finer grain size of tungsten particles.
2. Cobalt containing alloy shows superior elongation and impact values. This is attributed to higher solubility of tungsten in the matrix phase, higher volume fraction of the matrix and lower connectivity of the tungsten.
3. Rhenium added alloy exhibits highest ultimate tensile strength (1380 MPa), which may be attributed to the finer microstructure.
4. While sintered plus heat treated alloy shows lower strength and higher elongation, following swaging strength increases and elongation comes down. Additionally, work hardening exponent decreases following swaging.

Acknowledgments

Authors convey their sincere gratitude to Dr. Amol Gokhale,

Distinguished Scientist and Director, DMRL for encouragement and kind permission to publish this work. Authors gratefully acknowledge the financial support provided by DRDO. They would also like to thank the staff members of Powder Metallurgy Group, DMRL for their help in experimentation. Thanks are also due to G. B. Vikram, S. Venkat and Suneel for their help in tensile testing, microstructure and machining of samples.

References

[1] F.V. Lenel, F.V. Metal, Powder Industry Federation, Princeton (1980).
[2] R.M. German, L.L. Bourguignon, B.H. Rabin, Powder Metall. 5 (1992) 3–13.
[3] R. Gero, D. Chaiat, Mater. Eng. Conf. (1981) 46–50.
[4] R.M. German, Sintering Theory and Practice, Wiley, New York, 1996.
[5] S. Pappu, C. Kennedy, L.E. Murr, L.S. Magness, D. Kapoor, Mater. Sci. Eng. A 262 (1999) 115–128.
[6] F.E. Sczerzenie, H.C. Rogers, Hydrogen in metals, ASM, New York, 1974.
[7] L.G. Bazenova, A.D. Vasiljev, R.V. Minakova, V.J. Trefilov, Powder Metall. Int. 1 (1980) 45–51.
[8] B. Katavic, Sci.Sinter. 32 (2000) 153–166.
[9] S. Islam, F. Humail, M. Tufail, Int. J. Refract. Hard Mater 25 (2007) 380–385.
[10] R.M. German, L.L. Bourguignon, B.H. Rabin, J. Met. (1985).
[11] U. Ravi Kiran, M. Sankaranarayna, T.K. Nandy, Mater. Sci. Eng. A 582 (2013) 389–396.
[12] B. Katavic, M. Nikacevic 2nd, Int. Conf. Serb. Monten. Belgrad. (2005) 135–140.
[13] U. Ravi Kiran, M. Sankaranarayana, T.K. Nandy, Int. J. Refract. Hard Mater 33 (2012) 113–121.
[14] K.S. Churn, J.W. Noh, H.S. Song, E.P. Kim, W.H. Baek, In: Proc. Int. Conf. MPIF (1992) 397.
[15] ASTM E23-0a. Standard test methods for un-notched bar impact testing of powder structural parts, 2002.
[16] J. Ryu, H. Soon, H. Beak, Mater. Sci. Eng. A291 (2000) 91–96.
[17] H.H. Hausner, H.W. Antes, G.D. Smith, Met. Powder Ind. Fed. 14 (1981) 189–203.
[18] W. Zhou, X. Gao, Y.-G. Zhou, F.-H. Luo, Mater. Sci. Eng. Powder Metall. 15 (2010) 141–144.
[19] T.K. Kang, E.T. Henig, G. Petzow, MPIF (1981) 189–203.
[20] U. Ravi Kiran, M. Sankaranarayana, T.K. Nandy, Int. J. Refract. Hard Mater. 37 (2013) 1–11.